Probing how bright the quark-gluon plasma glows in lattice QCD

Ardit Krasniqi,[1,*] Marco Cè,[2,3] Tim Harris,[4] Renwick J. Hudspith,[5] and Harvey B. Meyer[1,6]

[1]*PRISMA+ Cluster of Excellence and Institut für Kernphysik, Johannes Gutenberg-Universität Mainz, D-55099 Mainz, Germany*

[2]*Dipartimento di Fisica "Giuseppe Occhialini," Università degli Studi di Milano-Bicocca, Piazza della Scienza 3, 20126 Milan, Italy*

[3]*Istituto Nazionale di Fisica Nucleare (INFN), Sezione di Milano-Bicocca, Piazza della Scienza 3, 20126 Milan, Italy*

[4]*Institute for Theoretical Physics, ETH Zürich, Wolfgang-Pauli-Strasse 27, 8093 Zürich, Switzerland*

[5]*Department of Physics, Carnegie Mellon University, Pittsburgh, Pennsylvania 15213, USA*

[6]*Helmholtz-Institut Mainz, Johannes Gutenberg-Universität Mainz, D-55099 Mainz, Germany*

(Received 21 May 2025; accepted 18 September 2025; published 10 October 2025)

Determining the spectrum of photons emitted by the quark-gluon plasma nonperturbatively remains an open computational challenge. In this paper, we calculate two moments of that spectrum at a tem-perature $T \approx 254$ MeV, employing lattice QCD with two flavors of $\mathcal{O}(a)$-improved Wilson fermions, without facing an inverse problem. Our central value for the difference of these two moments, which is sensitive to photon energies $\omega \gtrsim \pi T$, is lower than, but compatible with that obtained by integrating the leading-order weak-coupling photon spectrum. This study informs the "direct photon puzzle" in heavy-ion collision phenomenology, where it has proved difficult to simultaneously explain the yield and azimuthal anisotropy of photons not originating from final-state hadronic decays.

DOI: 10.1103/8dq9-q62p

I. INTRODUCTION

The radiation spontaneously emitted by a thermal medium provides important insight into its composition and dynamics. For instance, in astronomy, the spectral lines of interstellar gas are the main source of information on its constituents and overall motion [1]. In this paper, we are concerned with the photon emissivity of strongly interacting matter above the (crossover) transition temperature T_c. At asymptotically high temperatures, from a plasma of quasi-free moving quarks and gluons, a photon can only be emitted if a quark enters a collision, making the photon emissivity directly sensitive to interactions within the medium.

In relativistic heavy-ion collisions (HICs), the transverse-momentum-dependent yield and azimuthal anisotropy of direct photons[1] have been studied in several experiments [2–11]. These observables are sensitive to photon production throughout the spacetime history of the matter produced in the collision, and predicting them requires a complex modeling of the system's expansion and cooling. It has been difficult to explain the experimental measurements by the (otherwise very successful) hydrodynamic description and a model of the thermal photon emissivity [12] based on the leading weak-coupling prediction for the high-temperature phase. This open problem has been dubbed the direct photon puzzle [13–15].

The differential photon emissivity of a medium at perfect thermal equilibrium is, to leading order in the fine-structure constant α, proportional to a thermal spectral function $\sigma_{\mathrm{em}}(\omega)$, ω being the photon energy in the rest frame of the fluid. In this paper, we compute two energy moments of this spectral function at a temperature $T \approx 254$ MeV, i.e., around $1.2T_c$ [16] from first principles using lattice QCD. We compare our results with the moments obtained by integrating the full leading-order weak-coupling spectral function derived by Arnold, Moore, and Yaffe (AMY) from kinetic theory [17]. Our work tests the adequacy of the latter at temperatures typical of heavy-ion collisions. Thereby, it contributes to our theoretical understanding of thermal strong-interaction matter as well as to resolving the direct photon puzzle [13] of HIC phenomenology.

In contrast to previous lattice QCD studies of the photon emissivity [18–21], the present study does not involve tackling a numerically ill-posed inverse problem. It significantly improves upon our recent works [22,23] through superior statistical precision on the current-current

*Contact author: arkrasni@uni-mainz.de

[1]Direct photons are those that are not produced through the decay of final-state hadrons, as, for instance, in $\pi^0 \to \gamma\gamma$.

correlation functions, thereby allowing us to more stringently probe the emission of the phenomenologically most relevant photons, $\omega \gtrsim \pi T$.

II. FRAMEWORK

The differential rate of photon emission per unit volume plasma at temperature $T = 1/\beta$ can be expressed to leading order in α as [24]

$$\frac{\mathrm{d}\Gamma}{\mathrm{d}\omega} = \frac{\alpha}{\pi}\frac{2\omega\sigma_{\mathrm{em}}(\omega)}{e^{\beta\omega}-1}. \tag{1}$$

The photon spectral function $\sigma_{\mathrm{em}}(\omega)$ is rich in information about the thermal system. In particular, the electric conductivity is given by $\sigma_{\mathrm{el}} = 2\pi\alpha \lim_{\omega\to 0}\sigma_{\mathrm{em}}(\omega)/\omega$. In the Matsubara formalism of thermal field theory, in which the (imaginary) time variable is compact, $0 \le x_0 < \beta$, we define for each frequency $\omega_n = 2n\pi T$, $n \in \mathbb{Z}$, the correlation function of the vector current $j_\mu(x)$,

$$H_E(\omega_n) = \int \mathrm{d}^4x e^{\omega_n(ix_0 - x_1)}\left\langle j_3(x) j_3^\dagger(0)\right\rangle. \tag{2}$$

The quantity $H_E(\omega_n)$ has a spectral representation at fixed, lightlike virtuality [25],

$$H_E(\omega_n) = -\frac{\omega_n^2}{\pi}\int_0^\infty \frac{\mathrm{d}\omega}{\omega}\frac{\sigma(\omega)}{\omega^2+\omega_n^2}. \tag{3}$$

The difficulty of computing $H_E(\omega_n)$ increases dramatically with n due to the enhanced contribution at large spatial separations x_1, where the correlator suffers an exponential deterioration of the signal-to-noise ratio. The first moment $H_E(\omega_1)$ was determined with an uncertainty of 1% in Ref. [23]. Of particular interest is the difference of the $n = 2$ and $n = 1$ moments, since it suppresses the contribution of the very soft photons and is sensitive to the kinematically interesting region $\omega \gtrsim \pi T \approx 1$ GeV relevant to the direct photon puzzle. Therefore, we focus on the computation of the $n = 2$ moment in the following.

We use simulations with $N_{\mathrm{f}} = 2$ flavors of dynamical $\mathcal{O}(a)$-improved Wilson quarks with the Wilson gauge action (see the Appendix) and compute the correlator of the isospin current[2] $j_\mu \coloneqq (\bar{u}\gamma_\mu u - \bar{d}\gamma_\mu d)/\sqrt{2}$. The specific expression used in the lattice calculation is [23]

$$\begin{aligned} H_E(\omega_n) &= a^4\sum_x (e^{i\omega_n x_0} - e^{i\omega_n x_2})e^{-\Omega_n x_1}\left\langle j_3(x) j_3^\dagger(0)\right\rangle \\ &= \frac{a}{2}\sum_{x_1=-\infty}^{\infty} h_E(\omega_n, x_1), \\ h_E(\omega_n, x_1) &= 2[G_{\mathrm{ns}}^T(\omega_n, x_1) - G_{\mathrm{st}}^T(\omega_n, x_1)]\cosh(\Omega_n x_1), \end{aligned} \tag{4}$$

where G_{ns}^T and G_{st}^T denote nonstatic and static transverse screening correlators with momentum insertions along the temporal and spatial directions, respectively. In the continuum, the static contribution vanishes, but on the lattice it helps reduce discretization errors. Also, one may choose $\Omega_n = \omega_n(1 + \mathcal{O}(a^2))$ in order to suppress artifacts due to the finite lattice spacing a [26].

A one-parameter family of kernel regularizations is given by the choice

$$\Omega_n(k) = \frac{k}{a}\sin\left(\frac{a\omega_n}{k}\right), \qquad k \in \mathbb{R}. \tag{5}$$

In our final analysis, we include continuum extrapolations for $k = 2$, a choice motivated by the dispersion relation of a free lattice scalar field, and $k = 3/2$, which empirically yields the flattest continuum extrapolation (see Fig. 4, bottom panel). As a third variant for Ω_n, we opt for a smooth interpolation centered at $x_1 = \beta$ between the values ω_n at short distances and $\frac{1}{a}\sin(a\omega_n)$ at long distances. This choice is guided by a study of cutoff effects in leading-order lattice perturbation theory; see the Appendix.

Our lattice simulations are performed on three ensembles, labeled X7, W7, and O7, with lattice spacings $a = 0.033, 0.039, 0.049$ fm, tuned to a common temperature of $T \approx 254$ MeV. We achieve very high statistics on the relevant correlators: the propagators entering Eq. (4) are computed using "Z2SEMWall" [27–29] stochastic momentum [30] wall sources, within a truncated solver approach [31]. That is, we perform many more low-precision solves for translations in space across the lattice than high-precision ones. The DFL+SAP+GCR algorithm of [32] is used to solve the Dirac equation, whereby the cost of generating the deflation subspace is amortized by the large number of low-precision translations and stochastic "hits" we perform. The combination of stochastic momentum wall sources and the truncated solver method allows us to achieve much higher statistical resolution than the exact point sources previously employed in [23] with typically lower overall cost. The only limitation is that the momenta are fixed *a priori*.

We perform simultaneous, correlated continuum extrapolations for two out of the three datasets associated with a particular choice of Ω_n, enforcing a common continuum limit between them. For each of the three pairs, we consider four combinations depending on whether the coarsest

[2]For $j_\mu \coloneqq \frac{2}{3}\bar{u}\gamma_\mu u - \frac{1}{3}\bar{d}\gamma_\mu d + \cdots$, we have $\sigma_{\mathrm{em}} = \sigma$. With j_μ set to the isospin current, neglecting SU(3)-flavor breaking effects in the high-temperature phase, we have $\sigma_{\mathrm{em}} \simeq (\frac{4}{9} + \frac{1}{9} + \frac{1}{9})\sigma$.

lattice spacing ensemble labeled O7 is included or excluded independently in each extrapolation (i.e., both extrapolations include O7, only one includes O7, or both exclude it). This results in $3 \times 4 = 12$ fit models.

We average the results derived from these different choices according to the Akaike information criterion [33] and the model averaging method from Refs. [34,35]. The weight assigned to each fit is

$$w_i = N \exp\left[-\frac{1}{2}(\chi_i^2 + 2k_i - 2n_i)\right], \tag{6}$$

where k_i is the number of fit parameters and n_i is the number of data points in the fit with minimized χ_i^2. The normalization N is such that $\sum_i w_i = 1$. The central value and statistical uncertainty of an observable $\mathcal{O}$ are obtained via a weighted average over all models,

$$\bar{\mathcal{O}} = \sum_i w_i \mathcal{O}_i, \tag{7}$$

while the systematic error associated with the continuum extrapolation is estimated as

$$(\delta\mathcal{O})^2_{\text{sys}} = \sum_i w_i (\mathcal{O}_i - \bar{\mathcal{O}})^2. \tag{8}$$

The statistical uncertainties of our (derived) observables are estimated using the Γ method [36–38], as implemented in the PYERRORS package [39].

III. RESULTS

The numerical challenge to determine the moments $H_E(\omega_n)$ stems from (a) the exponentially deteriorating signal-to-noise ratio for the correlators at large distances x_1 and (b) the exponential enhancement of the tail by the kernel. As a result, the uncertainty of the integrand grows exponentially at large source-sink separations; see Fig. 1. However, it is known that both correlators G_i^T, $i \in \{\text{ns}, \text{st}\}$,

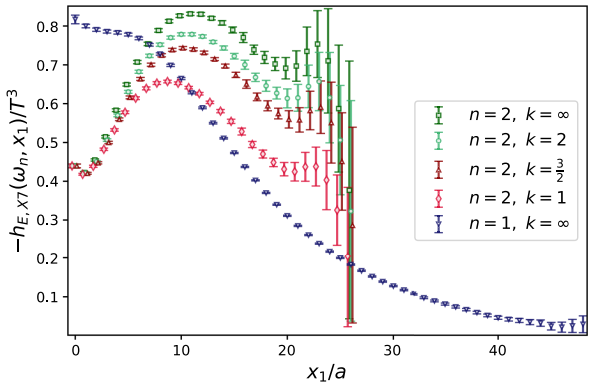

FIG. 1. Integrands $-h_E(\omega_2, x_1)$ with different kernel modifications based on the parameter k as well as $-h_E(\omega_1, x_1)$ on the finest ensemble X7.

are given at long distance (and in infinite volume) by a sum of exponentials with positive prefactors. Taking into account the periodic boundary conditions in our simulations, we employ the fit ansatz

$$G_i^T(\omega_n, x_1) = \sum_{l=0}^{2} |A_i^l|^2 \cosh[(x_1 - L/2) m_i^l(\omega_n)]. \tag{9}$$

The pairs m_i^l, A_i^l represent the lth screening masses and corresponding amplitudes in a given sector ω_n. The impact of including additional states in the fit ansatz (9) is illustrated in Fig. 6 (in the Appendix), where results from one-, two-, and three-state fits are compared.

The results for the ground states in the $n = 2$ sector, after taking the continuum limit, are

$$m_{\text{st}}^{0,\text{fit}}(\omega_2)/T = 14.73(26), \tag{10}$$

$$m_{\text{ns}}^{0,\text{fit}}(\omega_2)/T = 15.72(31). \tag{11}$$

The corresponding results for our finest ensemble are displayed in Fig. 2.

Since there is a systematic error associated with the choice of fit range and the number of states included, we also follow an alternative procedure where we include a prior in the fit. We obtain these priors by fitting the ratios of correlators $G_i^T(\omega_2, x_1)/G_i^T(\omega_1, x_1)$ to a single exponential. The thus extracted mass gap is shown in Fig. 3. When added to the screening mass associated with $G_i^T(\omega_1, x_1)$, it provides a suitable prior for the screening mass in the ω_2 sector. The continuum-extrapolated values of these priors are

$$m_{\text{st}}^{0,\text{ratio}}(\omega_2)/T = 14.07(18), \tag{12}$$

$$m_{\text{ns}}^{0,\text{ratio}}(\omega_2)/T = 14.99(21). \tag{13}$$

At the finest lattice spacing, the results from this procedure are illustrated in Fig. 2 with the green band.

The motivation for this alternative procedure is that the local effective masses, defined generically by

$$\frac{\cosh[(x_1 + a/2 - L/2) m_{\text{eff}}^{[G]}(x_1)]}{\cosh[(x_1 - a/2 - L/2) m_{\text{eff}}^{[G]}(x_1)]} = \frac{G(x_1 + a/2)}{G(x_1 - a/2)}, \tag{14}$$

resemble each other in the $n = 2$ and $n = 1$ sector. In the continuum and infinite-volume limit, the static screening mass is determined by the relativistic dispersion relation,

$$m_{\text{st}}^{0,\text{disp}}(\omega_2)/T = \sqrt{(m_{\text{st}}^0(\omega_0)/T)^2 + (4\pi)^2} = 13.96(2),$$

and this expectation is better fulfilled by the fits with priors. However, the difference between the two sets of results

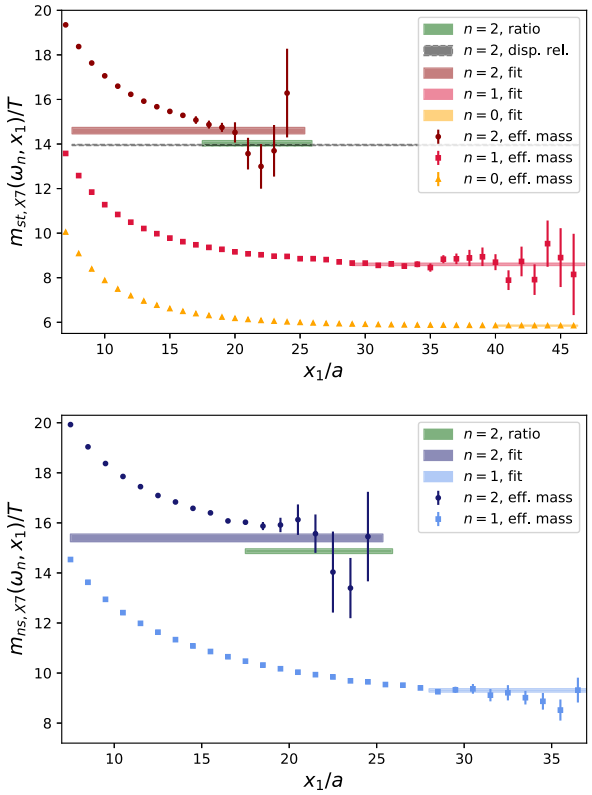

FIG. 2. Top: effective mass [see Eq. (14)] and fit results for the static correlators at spatial momenta ω_0, ω_1, and ω_2 on the X7 ensemble. Bottom: effective mass and fit results for the nonstatic screening correlator in the $n = 1$ and $n = 2$ Matsubara sector.

ultimately reflects the systematic uncertainty of describing the tail of the screening correlators. We expect these two methods to offer complementary estimates that bracket the true screening mass. We find the nonstatic screening mass in sector ω_2, $m_{\rm ns}^{0,\rm w/prior}(\omega_2)/T = 15.09(20)$ to be in good agreement with the Electrostatic QCD prediction of $m_{\rm ns}^{0}(\omega_2)/T = 15.0(2)$ [40].

Using our fitted values of m_i^l and A_i^l, we extend the lattice data for the correlators $G_i^T(\omega_2, x_1)$ beyond the reference

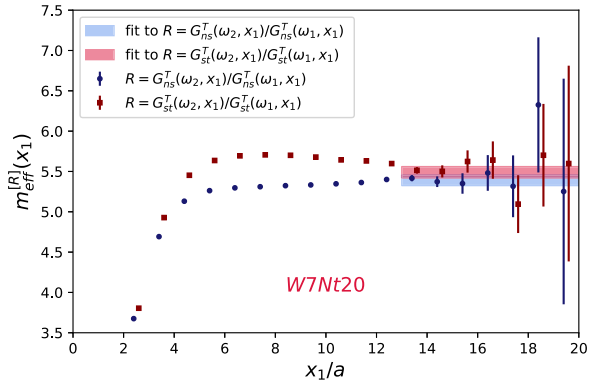

FIG. 3. Effective masses [see Eq. (14)] for the ratios of the $n = 2$ to the $n = 1$ Matsubara sector static (red bars) and nonstatic (blue bars) screening correlators on W7.

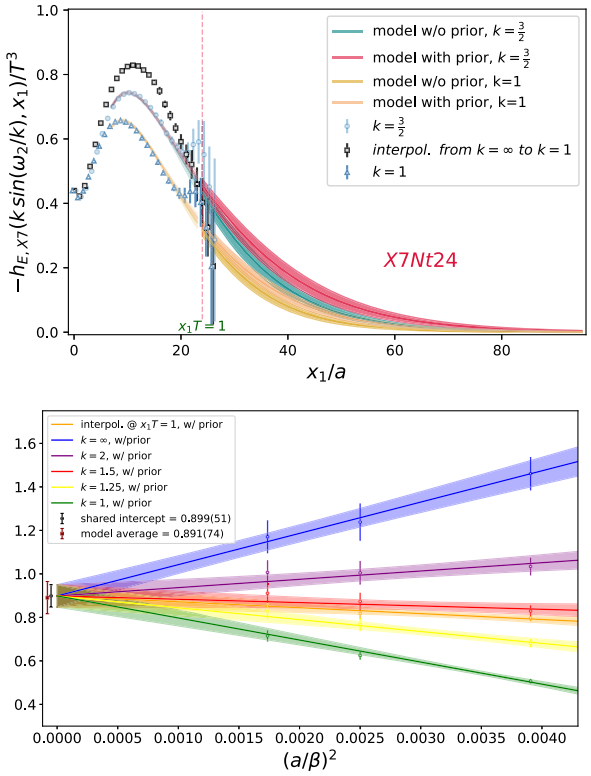

FIG. 4. Top: integrands $-h_E(\Omega_n(k), x_1)/T^3$ for $k \in \{1, \frac{3}{2}, \infty\}$ along with the interpolation between the prescriptions $k = \infty$ and $k = 1$ at $x_1T = 1$ and choosing $d \approx 0.15$ fm in Eq. (A1). The integrands are shown on the X7 ensemble together with the tail modification. Bottom: simultaneous (uncorrelated) continuum extrapolation with a shared intercept for $-H_E(\omega_2)/T^2$ using priors from the "ratio method." The result $[-H_E(\omega_2)/T^2]^{\rm uncorr}_{\rm w/prior} = 0.899(51)_{\rm stat}$ agrees well with our quoted MAV result, Eq. (15).

distance $x_1 = \beta$ as a sum of exponentials, as illustrated in the top panel of Fig. 4, in order to compute $H_E(\omega_2)$ according to Eq. (4). We perform separate model averages (MAVs) for the analyses performed without and with a prior, obtaining

$$[-H_E(\omega_2)/T^2]^{\rm MAV}_{\rm w/prior} = 0.891(24)_{\rm stat}(54)^{\rm cont}_{\rm sys}[59], \quad (15)$$

$$[-H_E(\omega_2)/T^2]^{\rm MAV}_{\rm w/o\,prior} = 0.846(27)_{\rm stat}(40)^{\rm cont}_{\rm sys}[48]. \quad (16)$$

The results in (15) and (16) agree well with those obtained from a simultaneous, uncorrelated continuum extrapolation using a common intercept across a range of k values; see Fig. 4, bottom panel. The systematic uncertainty is estimated via Eq. (8) and reflects the variation among continuum extrapolations obtained from different choices of Ω_n; see Eq. (5) and below.

As our final result, we quote the mean of Eqs. (15) and (16),

$$-H_E(\omega_2)/T^2 = 0.869(24)_{\rm stat}(54)^{\rm cont}_{\rm sys}(44)^{\rm tail}_{\rm sys}[74]_{\rm tot}, \quad (17)$$

where the systematic uncertainty related to the tail extension is taken as the full difference of 0.044(17) between the two results (15) and (16), which is statistically significant.

Our result is compatible with the previous result from [23] while having a smaller uncertainty. The vastly improved statistical precision, up to a factor 6.5 in the integrand at separations of $x_1 \approx \beta$ (see Fig. 5 in the Appendix), has enabled us to make a comprehensive study of the systematic uncertainties due to the large-x_1 contribution. Finally, subtracting the precisely determined first moment $-H_E(\omega_1)/T^2 = 0.676(7)$, we obtain

$$-[H_E(\omega_2) - H_E(\omega_1)]/T^2 = 0.193(74). \quad (18)$$

The same quantity evaluated from the AMY spectral function [17] lies in the interval [0.25, 0.30], depending on the value of the strong coupling $\alpha_s \in [0.25, 0.31]$ used. Thus, our result is on the low side of, but compatible with the weak-coupling prediction. Previous lattice studies [18–21] found photon emissivities in the quark-gluon plasma consistent with the AMY prediction, but we emphasize that ours is free of systematic uncertainties associated with an inverse problem and provides evidence at the 2.6σ level for a nonzero photon emissivity.

IV. CONCLUSION

By computing the second moment of the photon spectrum for quark-gluon plasma at a temperature around 254 MeV, we were able to probe the emissivity of hard photons and compare it to weak-coupling predictions. Our current result for $|H_E(\omega_2) - H_E(\omega_1)|$ is on the lower end of the corresponding leading-order prediction [17]; note that the next-to-leading-order correction is positive [41]. Furthermore, in our earlier study [42] we found that $|H_E(\omega_1)|/T^2$ near the crossover is comparable to that in the high-temperature phase, indicating sizable photon emission in this temperature regime corresponding to late times in heavy-ion collisions. These observations could shed light on the direct photon puzzle, since the azimuthal anisotropy of the photons rises if a larger fraction of the produced photons originate from the later stages of the collision [43]. It would thus be interesting to quantitatively study the impact of our findings concerning the thermal photon emissivity on the hydrodynamics-based predictions for the photon yield and anisotropy in heavy-ion collisions at RHIC and the LHC.

For generating the configurations and performing measurements, we used the OPENQCD [44] as well as the QDP++ packages [45], respectively.

ACKNOWLEDGMENTS

We thank Csaba Török for a pleasant collaboration [23] in the recent past, out of which this project grew. This work was supported by the European Research Council (ERC) under the European Union's Horizon 2020 research and innovation program through Grant Agreement No. 771971-SIMDAMA, as well as by the Deutsche Forschungsgemeinschaft (DFG, German Research Foundation) through the Cluster of Excellence "Precision Physics, Fundamental Interactions and Structure of Matter" (PRISMA+EXC 2118/1) funded by the DFG within the German Excellence strategy (Project ID 39083149). The research of M. C. is funded by the Italian Ministry of University and Research (MUR) through the "Rita Levi Montalcini" program for young researchers. R. J. H. acknowledges support from the U.S. National Science Foundation under Award No. OAC-2311430. The generation of gauge configurations was performed on the Clover and Himster2 platforms at Helmholtz-Institut Mainz and on Mogon II at Johannes Gutenberg University Mainz. We have also benefited from computing resources at Forschungszentrum Jülich allocated under NIC project HMZ21. The authors gratefully acknowledge the computing time provided to them on the high-performance computing cluster Noctua 2 at the NHR Center PC2, which is funded by the Federal Ministry of Education and Research and the state governments participating on the basis of the resolutions of the GWK for the national high-performance computing at universities [46].

DATA AVAILABILITY

The data that support the findings of this article are not publicly available upon publication because it is not technically feasible and/or the cost of preparing, depositing, and hosting the data would be prohibitive within the terms of this research project. The data are available from the authors upon reasonable request.

APPENDIX: SIMULATION SETUP AND ANALYSIS DETAILS

1. Simulation parameters and algorithmic aspects

Simulations were performed at a fixed temperature of $T \approx 254$ MeV and aspect ratio $L/\beta = 4$, with L (β) denoting the spatial (temporal) lattice extent. We use the local discretization of the vector current, which has support on a single lattice site. We renormalize the local vector

TABLE I. Overview of the $N_f = 2$ ensembles used in this study. The parameters given are the bare gauge coupling g_0, Wilson hopping parameter κ, lattice spacing a, temporal size β in units of the lattice spacing a, number of configurations used N_{con}, and number of inversions N_{inv}.

Label	$6/g_0^2$	κ	a (fm)	β/a	N_{con}	$\frac{N_{inv}^{\omega_1}}{10^7}$	$\frac{N_{inv}^{\omega_2}}{10^7}$
O7	5.5	0.13671	0.049	16	1400	2.15	8.60
W7	5.685727	0.136684	0.039	20	1600	1.54	4.61
X7	5.827160	0.136544	0.033	24	1500	1.73	5.18

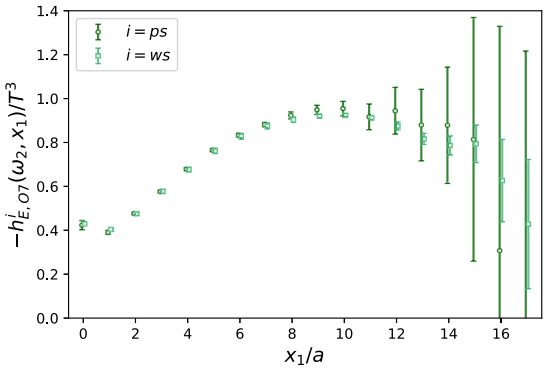

FIG. 5. Comparison of the integrand $-h_E^{\mathrm{ps}}(\omega_2, x_1)$ $(k = \infty)$ used in [23] with the integrand $-h_E^{\mathrm{ws}}(\omega_2, x_1)$ used in this work, on the coarsest ensemble O7. For instance, the error on $-h_E(\omega_2, x_1 = 15a)$ has been decreased by a factor of ≈6.5.

current by multiplying with $Z_V(g_0^2)$, with renormalization constants taken from from Ref. [47]. The ensemble parameters are summarized in Table I. The number of Dirac operator inversions is computed as

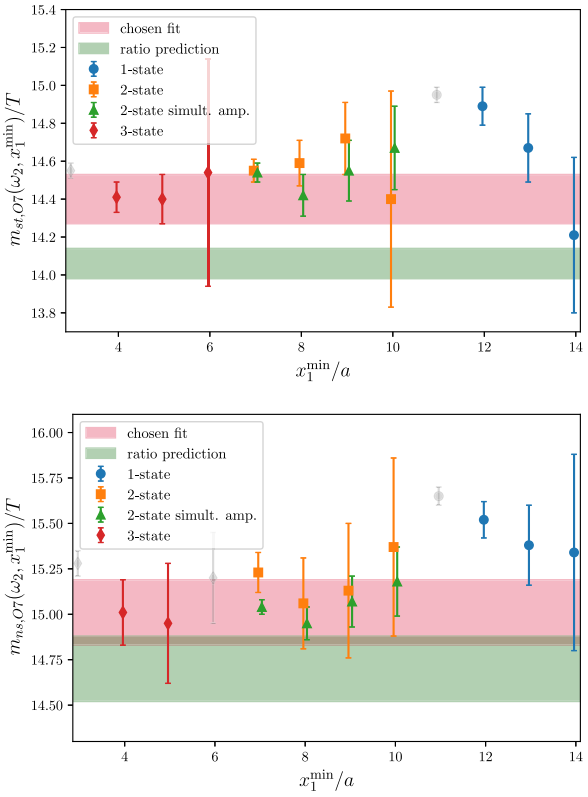

FIG. 6. Fit results along with the ratio prediction [finite lattice spacing pendant of Eqs. (12) and (13)] for the ground-state static (top) and nonstatic (bottom) screening masses in the second Matsubara channel on O7. The fit range is set by choosing $x_1^{\max}/a$ as the first point where the correlator is consistent with zero, while $x_1^{\min}/a$ is varied systematically. One-, two-, and three-state fits are shown; for the two-state case, simultaneous fits to static and nonstatic amplitudes are also included. Grayed-out points correspond to fits with p value > 0.95 or < 0.05.

$$N_{\mathrm{inv}} = N_{\mathrm{trans}} \times N_{\mathrm{hits}} \times N_{\mathrm{con}} \times N_p \times 4 \times 3,$$

where N_{trans} denotes the number of spatial translations (which we set to L/a), N_{hits} are the number of stochastic draws of the source, N_p is the number of momentum sources, the factor 4 is the number of spin indices, and 3 is the number of spatial decay directions we use. Note that no color dilution is applied. The impact on the integrand $h_E(\omega_2, x_1)$ of the improved statistical precision on the current-current correlators computed with wall sources (ws) instead of point sources (ps) is illustrated in Fig. 5.

2. Correlator fits: Varying the number of states

As a consistency check, we have fitted the static and nonstatic correlators in sector ω_2 with various numbers of states included in the ansatz (9). The impact of these variations on the lowest screening mass is illustrated in Fig. 6 for ensemble O7. Compatible results are found, provided the lower end $x_1^{\min}$ of the fit range is chosen sufficiently large.

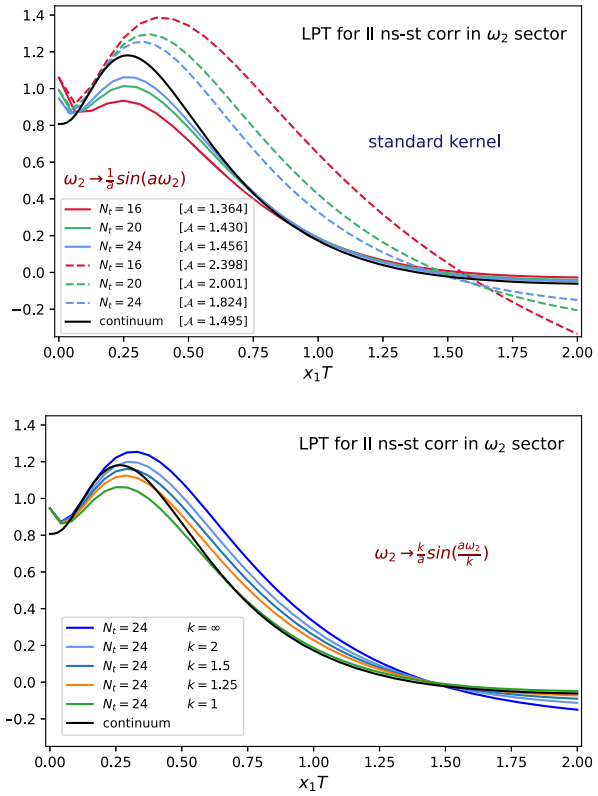

FIG. 7. Top: leading-order lattice perturbation theory (LPT) prediction for the standard subtracted correlator (using the local discretization of the vector current) with the cosh kernel (dashed lines) and with the modified ($k = 1$) sine kernel (solid line) in the free theory for the second Matsubara sector ω_2. Bottom: comparison of modifications with different k values for the $\beta/a = 24$ case.

3. Lattice perturbation theory and choice of kernel

In order to guide the choice of the kernel, we analyze the behavior of the integrand $h_E(\omega_2, x_1)$ in leading-order lattice perturbation theory with the local discretization of the current. Figure 7 (top panel) shows this quantity multiplied by the standard kernel (dashed lines) and the $k = 1$ kernel (solid lines), respectively. The standard kernel leads to large cutoff effects in the intermediate region $x_1 T \in [\frac{1}{3}, \frac{3}{2}]$, while the modified kernel ($k = 1$) reduces these substantially at $x_1 T > 3/4$.

Notably, with the standard kernel, the continuum limit is approached from above, whereas the modified kernel ($k = 1$) approaches it from below, which suggests a potential benefit of interpolating between them. We employ the smooth Heaviside function,

$$\Theta(x, x_w, d) = \frac{1}{2}\left[1 + \tanh\left(\frac{x - x_w}{d}\right)\right], \tag{A1}$$

to achieve a controlled transition between the two kernels: unmodified at short distances $x_1 < x_w$ and modified at long distances $x_1 > x_w$. For $d \approx 0.15$ fm, this results in a flat continuum extrapolation; see Fig. 4 (bottom panel). Additionally, the bottom panel of Fig. 7 compares different kernel modifications for the $\beta/a = 24$ case, corresponding to our finest ensemble, X7. It is evident that the modifications with $k = \frac{3}{2}$ and $k = 2$ also reduce cutoff effects, although neither performs as well as the $k = 1$ prescription.

[1] B. Draine, *Physics of the Interstellar and Intergalactic Medium* (Princeton University Press, Princeton, NJ, 2010).
[2] A. Adare *et al.* (PHENIX Collaboration), Phys. Rev. Lett. **104**, 132301 (2010).
[3] A. Adare *et al.* (PHENIX Collaboration), Phys. Rev. Lett. **109**, 122302 (2012).
[4] S. Afanasiev *et al.* (PHENIX Collaboration), Phys. Rev. Lett. **109**, 152302 (2012).
[5] A. Adare *et al.* (PHENIX Collaboration), Phys. Rev. C **91**, 064904 (2015).
[6] A. Adare *et al.* (PHENIX Collaboration), Phys. Rev. C **94**, 064901 (2016).
[7] N. J. Abdulameer *et al.* (PHENIX Collaboration), Phys. Rev. C **109**, 044912 (2024).
[8] N. J. Abdulameer *et al.* (PHENIX Collaboration), arXiv :2504.02955.
[9] L. Adamczyk *et al.* (STAR Collaboration), Phys. Lett. B **770**, 451 (2017).
[10] J. Adam *et al.* (ALICE Collaboration), Phys. Lett. B **754**, 235 (2016).
[11] S. Acharya *et al.* (ALICE Collaboration), Phys. Lett. B **789**, 308 (2019).
[12] C. Gale, J.-F. Paquet, B. Schenke, and C. Shen, Phys. Rev. C **105**, 014909 (2022).
[13] G. David, Rep. Prog. Phys. **83**, 046301 (2020).
[14] R. Chatterjee and P. Dasgupta, MDPI Phys. **6**, 674 (2024).
[15] C. Gale, arXiv:2502.13938.
[16] B. B. Brandt, A. Francis, H. B. Meyer, O. Philipsen, D. Robaina, and H. Wittig, J. High Energy Phys. 12 (2016) 158.
[17] P. B. Arnold, G. D. Moore, and L. G. Yaffe, J. High Energy Phys. 12 (2001) 009.
[18] J. Ghiglieri, O. Kaczmarek, M. Laine, and F. Meyer, Phys. Rev. D **94**, 016005 (2016).
[19] M. Cè, T. Harris, H. B. Meyer, A. Steinberg, and A. Toniato, Phys. Rev. D **102**, 091501 (2020).
[20] M. Cè, T. Harris, A. Krasniqi, H. B. Meyer, and C. Török, Phys. Rev. D **106**, 054501 (2022).
[21] S. Ali, D. Bala, A. Francis, G. Jackson, O. Kaczmarek, J. Turnwald, T. Ueding, and N. Wink (HotQCD Collaboration), Phys. Rev. D **110**, 054518 (2024).
[22] C. Török, M. Cè, T. Harris, A. Krasniqi, H. B. Meyer, and S. Ruhl, Proc. Sci., LATTICE2022 (**2023**) 193 [arXiv:2212.05622].
[23] M. Cè, T. Harris, A. Krasniqi, H. B. Meyer, and C. Török, Phys. Rev. D **109**, 014507 (2024).
[24] L. D. McLerran and T. Toimela, Phys. Rev. D **31**, 545 (1985).
[25] H. B. Meyer, Eur. Phys. J. A **54**, 192 (2018).
[26] H. B. Meyer, M. Cè, T. Harris, A. Toniato, and C. Török, Proc. Sci., LATTICE2021 (**2022**) 269 [arXiv:2112.00450].
[27] P. A. Boyle, A. Juttner, C. Kelly, and R. D. Kenway, J. High Energy Phys. 08 (2008) 086.
[28] P. Boucaud *et al.* (ETM Collaboration), Phys. Lett. B **650**, 304 (2007).
[29] C. McNeile and C. Michael (UKQCD Collaboration), Phys. Rev. D **73**, 074506 (2006).
[30] M. Gockeler, R. Horsley, H. Oelrich, H. Perlt, D. Petters, P. E. L. Rakow, A. Schafer, G. Schierholz, and A. Schiller, Nucl. Phys. **B544**, 699 (1999).
[31] G. S. Bali, S. Collins, and A. Schafer, Comput. Phys. Commun. **181**, 1570 (2010).
[32] M. Luscher, J. High Energy Phys. 07 (2007) 081.
[33] H. Akaike, *Information Theory and an Extension of the Maximum Likelihood Principle* (Springer Science+Business Media, New York, 1998).
[34] W. I. Jay and E. T. Neil, Phys. Rev. D **103**, 114502 (2021).
[35] S. Kuberski, M. Cè, G. von Hippel, H. B. Meyer, K. Ottnad, A. Risch, and H. Wittig, J. High Energy Phys. 03 (2024) 172.
[36] N. Madras and A. D. Sokal, J. Stat. Phys. **50**, 109 (1988).
[37] U. Wolff (ALPHA Collaboration), Comput. Phys. Commun. **156**, 143 (2004); **176**, 383(E) (2007).
[38] A. Ramos, Comput. Phys. Commun. **238**, 19 (2019).
[39] F. Joswig, S. Kuberski, J. T. Kuhlmann, and J. Neuendorf, Comput. Phys. Commun. **288**, 108750 (2023).

[40] B. B. Brandt, A. Francis, M. Laine, and H. B. Meyer, J. High Energy Phys. 05 (2014) 117.
[41] J. Ghiglieri, J. Hong, A. Kurkela, E. Lu, G. D. Moore, and D. Teaney, J. High Energy Phys. 05 (2013) 010.
[42] A. Krasniqi, M. Cè, T. Harris, R. J. Hudspith, H. B. Meyer, and C. Török, Proc. Sci., LATTICE2023 (**2024**) 180 [arXiv: 2401.05951].
[43] H. van Hees, C. Gale, and R. Rapp, Phys. Rev. C **84**, 054906 (2011).
[44] M. Lüscher and S. Schaefer, Comput. Phys. Commun. **184**, 519 (2013).
[45] R. G. Edwards and B. Joo (SciDAC Collaboration, LHPC Collaboration, and UKQCD Collaboration), Nucl. Phys. B, Proc. Suppl. **140**, 832 (2005).
[46] www.nhr-verein.de/unsere-partner.
[47] M. Dalla Brida, T. Korzec, S. Sint, and P. Vilaseca, Eur. Phys. J. C **79**, 23 (2019).